Journal of Magnetism and Magnetic Materials 471 (2019) 504–512

Contents lists available at ScienceDirect

Journal of Magnetism and Magnetic Materials

journal homepage: www.elsevier.com/locate/jmmm

Research articles

In-gel study of the effect of magnetic nanoparticles immobilization on their heating efficiency for application in Magnetic Fluid Hyperthermia

Matteo Avolio[a,*], Andrea Guerrini[b], Francesca Brero[a], Claudia Innocenti[b], Claudio Sangregorio[b,c], Marco Cobianchi[a], Manuel Mariani[a], Francesco Orsini[d], Paolo Arosio[d], Alessandro Lascialfari[d]

[a] Dipartimento di Fisica, INFN and INSTM, Università degli Studi di Pavia, Via Bassi 6, 27100 Pavia, Italy
[b] Dipartimento di Chimica and INSTM, Università degli studi di Firenze, Via della Lastruccia 6, Sesto F.no (FI), Italy
[c] ICCOM-CNR, Via della Lastruccia 6, Sesto F.no(FI), Italy
[d] Dipartimento di Fisica, INFN and INSTM, Università degli Studi di Milano, Via Celoria 16, 20133 Milano, Italy

ARTICLE INFO

Keywords:
Magnetic Fluid Hyperthermia
Magnetic nanoparticles
Superparamagnetism
Specific Absorption Rate
Relaxation times
Brownian motion

ABSTRACT

Recent studies on magnetic nanoparticles (MNPs) used for Magnetic Fluid Hyperthermia treatments have shown that Brownian rotation is suppressed when they are confined within a cell. To investigate this effect we conducted a systematic study of the Specific Absorption Rate (*SAR*) of colloidal suspensions of MNPs in water and gels at different agarose concentration. *SAR* measurements were conducted by varying the frequency (f = 110–990 kHz) and amplitude (up to 17 kA/m) of the applied alternating magnetic field (AMF). MNP samples with different diameter (d = 10, 14, and 18 nm) were used. Our results show that Néel relaxation dominates *SAR* with negligible contribution from Brownian motion for smaller MNPs (d = 10 nm). For the largest MNPs (d = 18 nm) we observed a more significant *SAR* decrease in gel suspensions as compared to those in solution. In particular, when applying AMFs as the ones used in a clinical setting (16.2 kA/m at f = 110 kHz), we measured *SAR* value of 67 W/g in solution and 25 W/g in gel. This experimental finding demonstrates that investigation of MNPs properties should be conducted in media with viscosity similar to the one found in mammalian tissues.

1. Introduction

Hyperthermia is an antitumoral therapy consisting in a temperature rise up to 43 °C, with the aim of damaging cancer cells by denaturating their basic molecular structures, such as DNA or enzymes [1,2]. This aim is achieved for instance by the so-called Magnetic Fluid Hyperthermia (MFH), that employs magnetic nanoparticles (MNPs), with the advantage of producing the temperature rise only within the neoplastic region where they are located. In this technique, colloidal solutions of biocompatible MNPs dispersed in physiological liquids and injected e.g., directly inside the tumour, release heat once exposed to an alternating magnetic field (AMF) operating at safe values of frequency and amplitude [3,4].

In most cases, for in vivo applications, MNPs consist of a magnetic core made of iron oxides, known to have a low toxicity [3,5], coated by organic biocompatible moieties. The core size is generally so small (the equivalent diameter typically is less than 20 nm) that the MNPs result to be superparamagnetic [1,6,7]. In the superparamagnetic regime the MNPs magnetization, also called superspin, can fluctuate between the two opposite directions of the easy axis determined by the magnetic anisotropy, with a characteristic relaxation time, τ_N. According to the Néel model for non-interacting particles τ_N depends on the core volume of the particles (V), the anisotropy constant (K_a) and the temperature of the system (T), and its expression is given by the Arrhenius law:

$$\tau_N = \tau_0 e^{K_a V/(k_B T)} \quad (1)$$

In Eq. (1) τ_0 is generally assumed of the order of 10^{-9} s [8,9] and k_B is the Boltzmann constant.

In a solvent the superspin orientation can change also through the physical process of rotation of the entire particle, which occurs in a characteristic time called Brown relaxation time τ_B [10] expressed by:

$$\tau_B = \frac{3\eta V_h}{k_B T} \quad (2)$$

where V_h is the hydrodynamic volume of the particles and η *is* the local viscosity of the medium. Thus, an effective relaxation time τ that accounts for both Néel and Brown mechanisms can be defined as:

* Corresponding author.
E-mail address: matteo.avolio01@universitadipavia.it (M. Avolio).

https://doi.org/10.1016/j.jmmm.2018.09.111
Received 22 June 2018; Received in revised form 21 September 2018; Accepted 28 September 2018
Available online 29 September 2018
0304-8853/ © 2018 Elsevier B.V. All rights reserved.

$$\frac{1}{\tau} = \frac{1}{\tau_N} + \frac{1}{\tau_B} \quad (3)$$

and the faster one results to be dominant in determining the spin dynamics [8,11,12].

The application of an AMF allows the MNPs to transfer energy to the colloidal solution (or, in vivo, to the patient tumour cells) through the Néel and Brown relaxation mechanisms. In particular, MNPs can release heat because of the energy loss due to the opening of the hysteresis loop that occurs when a dephasing between the particles' superspin and the external field at a specific frequency sets in [13]. This frequency is determined by τ, obtained from Eq. (3).

The Specific Absorption Rate (*SAR*) quantifies the heat released per unit mass of MNPs [14]. By following different heuristic or theoretical models (see Section 3), the analytical expression of this parameter results to depend on the particle size, the static magnetic properties and the spin dynamics [15]. As concerns the dynamics of MNPs in solution with organic coating thickness of few nanometers, when the iron-oxide core diameter is smaller than $d \approx 15$ nm [8] the Néel relaxation is generally the dominant mechanism. Above this diameter the Brownian rotation becomes increasingly more important until at $d \approx 20$ nm largely dominates. Remarkably, recent *in vitro* and *ex vivo* studies have shown that MNPs are mostly immobilized when injected into the tumour [16–19], and thus the Brownian rotation seems to be hindered when performing MFH treatment [20,21]. On the other hand, most of published papers on MFH report experiments on MNPs in solutions where, however, the Brownian relaxation can play an important role. This can induce misleading conclusions about the real heating efficiency of these systems when used for MFH on patients [16,22–24].

To systematically study the effect of the core size on the *SAR*, in this work we studied the chemico-physical properties of three samples of MNPs with magnetite (Fe_3O_4) core diameter $d \approx 10$, 14 and 18 nm, and measured the *SAR* at different frequencies (from 110 to 990 kHz) and intensities (up to 17 kA/m) of the applied AMF. Measurements were carried out both in water solution and in agarose gels with different mass fractions (0.5% and 2%), thus reproducing experimental conditions similar to the ones of tumour tissues with different viscosity and porosity, where Brownian relaxation is partially or totally suppressed [16–18,22,25].

Our results are aimed to complement information already reported elsewhere [16,22–28], through the investigation of the heating efficiency of magnetite MNPs as a function of their size in conditions closer to the biological ones.

2. Materials and methods

2.1. MNPs synthesis and their morpho-dimensional characterization

The three samples of magnetic nanoparticles were synthetized using the thermal decomposition method described by Cobianchi et al. [27]. In order to remove the Oleic Acid (OA) coating and suspend the MNPs in water, a ligand exchange was performed by reacting 20 mg of MNP@OA suspended in toluene 5 mg/mL with 10 mg of *meso*-2,3-dimercaptosuccinic acid (DMSA) solved in 2 mL of Dimethyl sulfoxide (DMSO). MNPs suspension were mixed with the DMSA solution and sonicated for 1 h, and then held in mechanical agitation for 24 h. At the end of the reaction the MNPs were separated magnetically, washed with ethanol two times and then suspended in water (10 mg/mL). To stabilize the colloidal solution pH were adjusted to 8 with addition of 0.1 M of NaOH solution.

Powder X-ray diffraction (XRD) measurements were carried out using a Bruker D8 Advance diffractometer equipped with Cu Kα (1.54178 Å) radiation and operating in $\theta - 2\theta$ Bragg − Brentano geometry at 40 kV and 40 mA, to determine the iron oxide phases and the crystal sizes.

Dynamic Light Scattering (DLS, Malvern Zetasizer ZS, Malvern Instruments Ltd., UK) measurements, Z-potential analysis and size distributions, were carried out onto 0.5 mg/mL suspension of the samples.

A CM12 PHILIPS Transmission Electron Microscope (TEM) operating at 100 kV using a LaF_6 source was used to evaluate the MNPs core sizes and shapes. Samples were prepared by drop casting a dilute toluene solution of MNPs onto 200 mesh carbon-coated copper grids. The recorded micrographs were processed by the iTEM TEM Imaging Platform software (Olympus), and were further analysed with the FIJI open software. The mean diameter and size distribution of the sample was obtained from a statistical analysis over 600 MNPs.

The total dimensions of the MNPs, including their organic coatings, were instead measured by Atomic Force Microscopy technique (AFM), using a Bruker Nanoscope Multimode IIId AFM system, operating in tapping-mode in air. The latter measurements were performed using silicon rectangular cantilever (NSG01, NT_MDT), with a declared length of 120 μm, a spring constant of 2.5 N/m and a resonance frequency of about 130 kHz. The samples were prepared by drying a drop of very diluted aqueous solution of MNPs on a Mica substrate. The mean diameters and size distributions were obtained from a statistical analysis over ~ 25 MNPs.

2.2. Magnetic measurements

The magnetic characterization of MNPs water suspensions (with Fe_3O_4 concentration c = 3 mg/mL) was performed by means of a SQUID Quantum Design MPMS magnetometer. Samples were sealed in a small capsule of polycarbonate and the measurements performed for $T \leq 260$ K, i.e., on frozen solutions. The signal of the empty sample holder was measured and subtracted to the total signal; moreover, the diamagnetic contribution of the water was removed. Hysteresis loops were acquired at low ($T = 2$ K) and high ($T = 260$ K) temperatures in the field range from −5 T to 5 T. Zero-Field-Cooled and Field-Cooled (ZFC – FC) curves were collected under a small magnetic field (5 mT) for each sample from 2 K to 260 K, thus keeping the samples in the frozen state during the whole experiment.

2.3. Hyperthermia measurements

The MNPs samples were prepared for hyperthermia measurements both in aqueous solution and in agarose gel. In order to evaluate the effects caused by the agarose concentration and consequently by the medium viscosity, two gels with different agarose mass fractions (0.5% and 2% w/w) were prepared. The agarose was added to the aqueous suspensions of MNPs and the sample heated up to the boiling point while mixing it with a pipette. This method doesn't allow to completely exclude the presence of very small ($d < 50$ nm) MNPs aggregates, neither in gel nor in water samples. Both gels simulate soft tissues in the body, with a different level of porosity and hardness [29]. Detailed information about the rheological properties of agarose gels can be found in literature [30,31], where the viscosity of the gels was estimated to be at least two order of magnitude higher than the one of pure water, and their melting temperature, always higher than 75 °C, was reported to increase with the agarose concentration. The magnetite concentration in the prepared samples was 10 mg/mL for the 10 nm and 14 nm samples, and 3 mg/mL for the 18 nm sample.

Magnetic Hyperthermia experiments were performed using a MagneTherm™ set-up by Nanotherics, working at five different field frequencies (109.8 kHz, 329.6 kHz, 524.2 kHz, 741.6 kHz and 990.5 kHz) and amplitudes (up to 17 kA/m). Due to the power limitation of the system, the maximum amplitude of the available AMF decreases with increasing the working frequency. Most of the field values chosen for the measurements satisfied the Brezovich criterion for the safe application of a magnetic field to a patient [32], and all of them fulfil the criterion reported by R. Hergt and S. Dutz [33].

A home-made thermalization system, based on a Lauda Alpha A thermostat, and a polystyrene sample holder were placed inside the

MagneTherm™ coil to stabilize the initial temperature of the sample to a fixed value of 25 °C. This system allows reproducible hyperthermia measurements using a very small amount (approximately 200 μL) of MNPs suspension.

The temperature of the samples was measured using an Optocon™ optical fibre thermometer carefully positioned at the centre of the sample placed inside an Eppendorf PCR Tube and centred in the middle of the coil. The sample centering in the middle of the coil was carefully adjusted to ensure the reproducibility of the magnetic field values on the sample itself. The temperature was acquired for 5 or 15 mins at steps of 0.1 s or 1 s, depending on the total increment. The contribution to the sample temperature rise coming from the overheating of the coil was estimated by measuring the increase of temperature in a sample made of pure water or gel in the same experimental conditions. It is known from literature [34] that the heat conductivity of agarose gels differs slightly from the one of water, being about 1.5% lower in the temperature range from 303 K to 323 K at 0.5% agarose concentrations, and about 9% lower at 5% agarose concentration. This small difference in the heat conductivity of the water and gel samples at the low agarose concentrations used for the measurements has been considered largely included in the uncertainty assumed for the *SAR* values (see Section 4.3). Finally, it has been verified that the rate of the temperature increment does not depend significantly on the initial temperature of the sample.

3. Magnetic fluid hyperthermia models

To describe the MFH heating efficiency of MNPs with different microscopic characteristics several models have been proposed [15].

The Linear Response Theory (LRT) can be applied to superparamagnetic nanoparticles when the magnetic energy is much lower than the thermal one. This condition can be explicated by imposing $\xi < 1$, where $\xi = \mu_0 M_{S_V} V H_{max}/k_B T$, being μ_0 the vacuum permeability, M_{S_V} the volumetric saturation magnetization and H_{max} the maximum amplitude of the applied AMF [15]. The LRT predicts that the *SAR* increases with the square of the maximum applied field H_{max} and is linear with the out-of-phase component $\chi''(f)$ of the magnetic susceptibility [9] of the sample:

$$SAR = \mu_0 \pi \chi''(f) f \frac{H_{max}^2}{C} \tag{4}$$

where f is the AMF frequency and C is the magnetite concentration inside the sample. According to the Debye's theory [8,32,35], for $\xi << 1$ the out-of-phase component of χ is expressed by:

$$\chi''(f) = \frac{\mu_0 M_{S_V}^2 V \phi}{3 k_B T} \frac{2\pi f \tau}{1 + (2\pi f \tau)^2} \tag{5}$$

with ϕ the volumetric fraction of magnetic material in the sample [8] and 3 is a factor introduced because of the random orientation of the MNPs easy-axes [15].

For larger single-domain MNPs that fall in the blocked regime, the LRT doesn't hold anymore. For $H_{max} > 2H_C$, where H_C is the coercive field of the MNPs [15], to evaluate the *SAR* from the area of the hysteresis loop the Stoner-Wohlfarth model can be applied. If $H \leq H_C$, for multidomain MNPs the Rayleigh model holds and it predicts an increase of *SAR* with the third power of H_{max}. In the transition region between the superparamagnetic and the multidomain regime, it has been theoretically [15] and experimentally [27] shown that the *SAR* follows a power law $SAR \propto H^x$ with $2 < x < 3$, i.e., in between the LRT and Rayleigh model predictions.

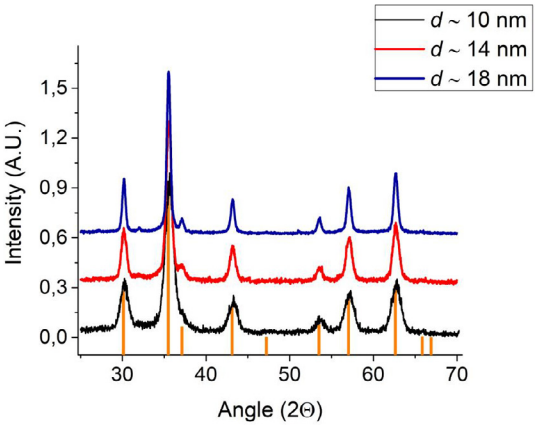

Fig. 1. XRD patterns of the three samples of MNPs with different diameter *d*, compared to the reference pattern (orange vertical bars) of magnetite (PDF 65-3107). (For interpretation of the references to colour in this figure legend, the reader is referred to the web version of this article.)

4. Results and discussion

4.1. Estimation of MNPs size from XRD, TEM, AFM, and DLS.

The X-Ray diffraction analysis (XRD), shown in Fig. 1, confirmed the face centred cubic (fcc) crystalline structure typical of inverse-spinel such as magnetite and maghemite with no evidence of other crystalline phases (wüstite, hematite). The crystalline size and the value of the lattice parameter a (Table 1), i.e., the physical dimension of the unit cell of the crystal lattice, were estimated by the Pawley method refinement [36] by setting the structure of the magnetite (Fd-3 m) with T.O.P.A.S.® software [37]. The a-values indicate that samples are made of magnetite (a = 8, 3970Å) rather than maghemite (a = 8, 3515Å).

The distributions of the core size of the three samples as obtained by TEM images analysis are reported in Fig. 2(a). Histograms were fitted using a Log-Normal function, and the mean values and standard deviations of the related Normal distributions were computed according to the formulas reported by Rosensweig [8]. Results are shown in Table 2; according to the mean value of the MNPs core diameters, the three samples will be named as 10 nm, 14 nm and 18 nm in the following of the article.

TEM images (Fig. 2(a)) show a very narrow distribution and a spherical shape for 14 nm sample; the other two samples appear more polyhedral and with a larger distribution of the core size. Moreover, the comparison between the core size seen by TEM (Table 2) and the crystal size seen by the XRD analysis (Table 1) certifies the monocrystalline nature of the MNPs.

A similar analysis was performed on the AFM images (Fig. 2(b)) that, as the technique measures the total diameter of the MNP, showed values for the MNPs diameters (Table 2) bigger than the ones obtained from the TEM analysis, due to the presence of the DMSA coating (DMSA thickness of about 1 or 2 nm). Aggregates in the AFM images are due to the drying process during the sample preparation. AFM analysis was performed on single particles, while aggregates were discarded.

DLS measurements on the three samples (Table 2) exclude the presence of aggregates, since the larger values obtained for the MNPs

Table 1
Crystal size and lattice parameter a obtained by fitting the XRD patterns with the Pawley [36] method using T.O.P.A.S.® software [37].

Sample	Crystal size (nm)	Lattice parameter a (Å)
10 nm	9.3	8.407(3)
14 nm	13.8	8.391(1)
18 nm	17.2	8.398(1)

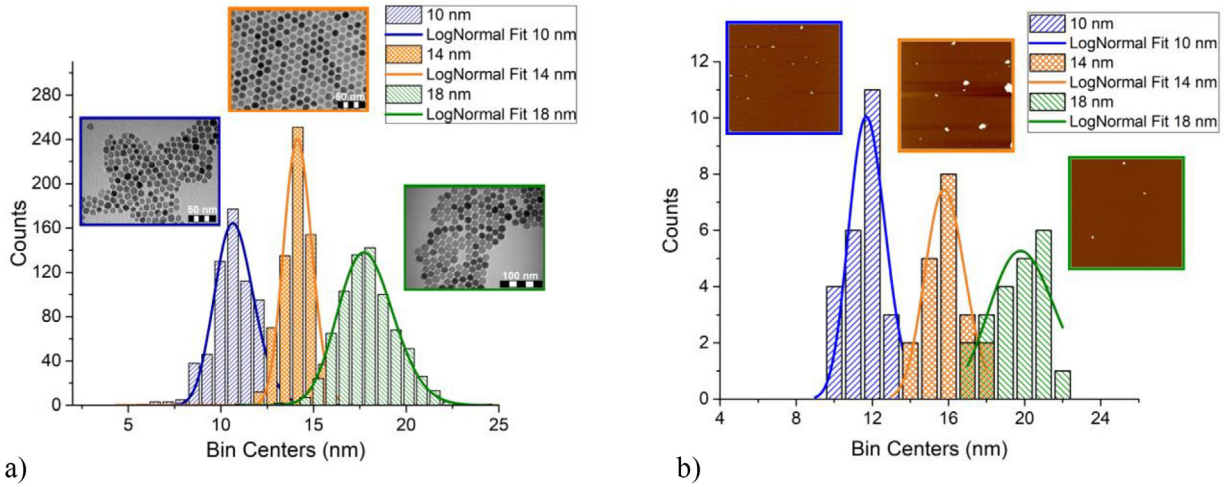

Fig. 2. (a) TEM images and histograms reporting the number of particles with a given core size for the three MNPs samples. (b) AFM images (2x2 μm^2) and histograms reporting the number of particles with a given hydrodynamic diameter (including the coating thickness) for the three MNPs samples. The three distributions are in both cases fitted with a Log-Normal function; the mean value and the standard deviation of the distribution are reported in Table 2.

Table 2
Mean MNPs diameters (and errors) obtained from the statistical analysis of TEM and AFM images and from DLS measurements for the three samples.

Sample	d_{TEM} (nm)	d_{AFM} (nm)	d_{DLS} [PDI] (nm)
10 nm	10.8 ± 0.8	11.6 ± 1.0	15.8 [0.379]
14 nm	14.2 ± 0.5	16.0 ± 1.1	21.4 [0.371]
18 nm	17.9 ± 1.5	19.7 ± 1.5	34.1 [0.319]

diameters with this technique can be related to the first water coordination spheres linked to the MNPs surface and to the dynamic nature of the measurement. The clear negative value of the Z-potential measured for all the samples (≈ −20 mV) confirmed a good stability of the colloidal solutions.

4.2. Magnetic measurements

In Fig. 3(a), the hysteresis loops acquired at low temperature ($T = 2$ K) on the three samples of MNPs in aqueous frozen solution are shown. In the left inset the details of the loops at low fields, particularly useful to evaluate the coercive field H_C and the remanence M_R, are reported. In the right inset, the magnetization curves of the three samples at high temperature ($T = 260$ K) are displayed. In this case, the coercivity is negligible, suggesting that the three samples are close to the superparamagnetic regime. The Saturation Magnetization M_S of the samples was evaluated by fitting the Langevin function [15] to the first magnetization curves, although systems near the blocking temperature are expected to not follow the behaviour typical of a paramagnetic system (see Refs. [38,39]).

The values of the saturation magnetization for the three samples are listed in Table 3, at low ($T = 2$ K) and high temperature ($T = 260$ K, low enough to keep the samples in the frozen state). The 18 nm sample shows the highest value of M_S, near to the value of the bulk magnetite ($91.7 Am^2/kg_{Fe_3O_4}$ at room temperature) [40]. In Table 3 the values of the coercive field at $T = 2$ K are also reported.

The ZFC-FC curves reported in Fig. 3(b) show interesting features: the 10 nm sample has a maximum in the ZFC curve at $T_{max} = 143$ K, which signs the transition from the high-T superparamagnetic behaviour to the blocked state [41]. The broadness of the peak suggests a quite large distribution of the MNPs core size as observed from the TEM images in Fig. 2(a). The 18 nm sample doesn't show any maximum in the ZFC curve, but shows a sharp increase at $T_V \approx 111$ K which can be associated to the Verwey transition, a typical phase transition of bulk magnetite. This transition temperature is lower than the one typically

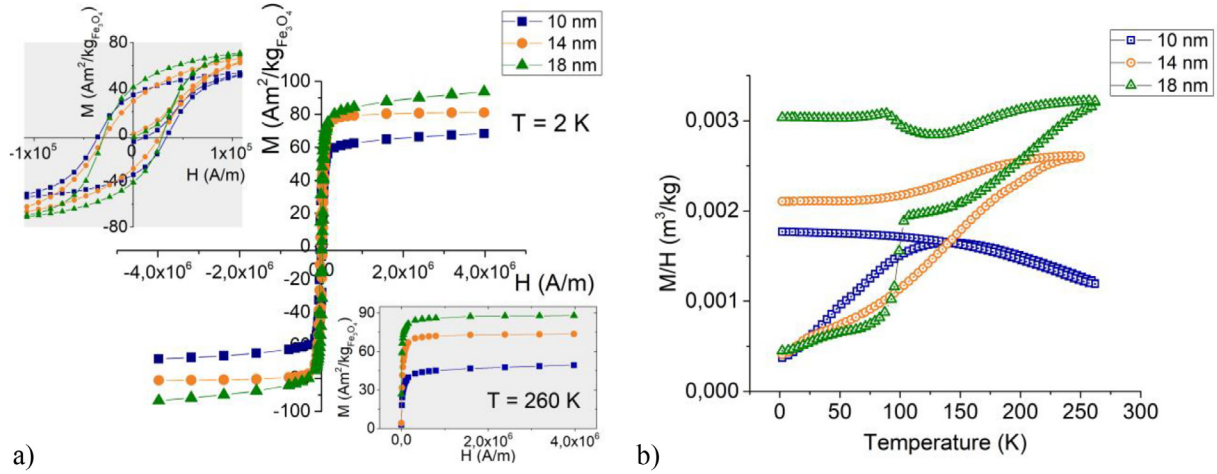

Fig. 3. (a) Hysteresis loop at low temperature ($T = 2$ K) of the three samples in aqueous frozen solutions: in the left inset the opening of the loop is evidenced; in the right inset the magnetization curves of the three samples at high temperature are reported. (b) Zero-Field-Cooled and Field-Cooled (ZFC-FC) M/H curves collected at low fields for the three frozen solution samples.

Table 3
Saturation magnetization (M_S) and coercive field (H_C) of the three samples in frozen solution at low and high temperatures.

Sample	M_S at 2 K ($\mathbf{Am^2/kg_{Fe_3O_4}}$)	H_C at 2 K (**kA/m**)	M_S at 260 K ($\mathbf{Am^2/kg_{Fe_3O_4}}$)
10 nm	69.3 ± 3.8	34.6 ± 1.7	51.1 ± 2.8
14 nm	81.6 ± 4.5	27.8 ± 1.4	74.1 ± 4.1
18 nm	96.2 ± 5.2	29.6 ± 1.5	88.3 ± 4.8

observed for bulk magnetite ($T_V^{bulk} \approx 125$ K), as indeed already observed for MNPs of decreasing size [42]. The decrease of T_V was ascribed to the presence of impurities and to a certain degree of non-stoichiometry of the magnetite [43–45]. For the 14 nm sample the Verwey transition is not identifiable, possibly because of the oxidation to maghemite of the surface layer in solution.

4.3. Magnetic Hyperthermia results

The temperature increasing rate of the samples was evaluated by applying the initial-slope method, based on the fitting of the acquired $T(t)$ curves with a straight line in a short time range; the fit starts few seconds after the application of the magnetic field to account for the thermal inertia of the system [6] (i.e., after about an interval of 5 to 20 s). When the increase rate was too slow and negatively influenced the precision of this method, the entire $T(t)$ curves were fitted to the Box-Lucas model $T(t) = A(1-e^{-Bt})$ [46,47]. The ratio $\Delta T/\Delta t$ for $t \to 0$ was directly evaluated in the first case, and by the product $A{\cdot}B$ in the second. The reproducibility of the results was checked by repeating the temperature acquisition runs up to 10 times.

The *SAR* of the samples was calculated using the following formula [48]:

$$SAR = \frac{m_{H_2O} c_{H_2O} + m_{Fe_3O_4} c_{Fe_3O_4}}{m_{Fe_3O_4}} \cdot \frac{\Delta T}{\Delta t} \tag{6}$$

where m_{H_2O} and $m_{Fe_3O_4}$ are, respectively, the mass of water and magnetite in the colloidal solutions, while $c_{H_2O} = 4.18\ \mathrm{JK^{-1}g^{-1}}$ and $c_{Fe_3O_4} = 0.62\ \mathrm{JK^{-1}g^{-1}}$ are the corresponding specific heat. We neglected the contribution of the DMSA coating because of its small mass fraction. In the case of MNPs samples in gel, the water contribution in the first term of the formula should be replaced by the agarose gel contribution. However, the difference of the specific heat between agarose gel and water at the concentration near to the ones used in this work (0.5% and 2%) is negligible ($c_{agar1\%} = (4.18 \pm 0.05)\ \mathrm{JK^{-1}g^{-1}}$ [23]). By considering the uncertainties on the quantities of Eq. (6), a standard deviation of about 10% on the *SAR* values was estimated. It should be noted that a (presumably slight) inhomogeneous distribution of MNPs inside the gel should not lead to such high differences between the $\Delta T/\Delta t$ ratios estimated for the water and gel samples.

The *SAR* values obtained from Eq. (6) by applying AMF of different frequencies and amplitudes are reported in Fig. 4; it should be noted that in our experimental set up the maximum amplitude field achievable depends on the applied frequency. For (H, f) values that produce a very low heating, the data are not reported, as e.g., in the case of 10 nm sample at $H_{max} = 3.5$ kA/m and $f = 990.5$ kHz.

In Fig. 4 it is possible to evince at least three important indications related to the supposed capability of the gel to immobilize the MNPs. First, the *SAR* values obtained for all the samples in the two agarose gels with mass fractions 0.5% and 2% are almost the same at all frequencies: this clearly indicates that the effect of MNPs immobilization doesn't change when the viscosity of the gel is increased. Then, the 10 nm sample doesn't show any substantial difference of *SAR* if measured in water or in agarose gel, thus suggesting that for this sample the contribution of the Brownian relaxation is negligible compared to the Néel one. Finally, the 14 nm and 18 nm samples show a relevant difference between the *SAR* values obtained in water and in the two gels (the latter being from 30% to 75% lower). In the last two cases, it is thus reasonable to suppose a sizeable influence of the Brown relaxation mechanism on the heat release, as expected for large particles [8].

These results are indeed in good agreement with the ones obtained in Ref.[22] where a similar systematic study of MFH, but performed just at one frequency (522 kHz) on maghemite ($\gamma{-}Fe_2O_3$) nanoparticles with different core sizes (6–14 nm) dispersed both in water and in agarose gel with 1% mass fraction, showed a significant decrease of *SAR* for MNPs larger than 13 nm when suspended in gel. Moreover, in another paper Di Corato et al. [16] demonstrated that *SAR* decreases consistently when measured *in vitro* with MNPs internalized by cells or immobilized on the cell membranes.

As additional result, Mehdaoui et al. [49] warned that a minor value of *SAR* for MNPs dispersed in gel compared to the ones in solution sometimes cannot be explained just by considering the suppression of the Brownian motion. In fact, MNPs in solutions can form chain-like structures thus increasing the inter-particle dipolar interaction, which contributes to the *SAR* increase (see Branquinho et al. [50] for theory and Serantes et al. [51] for experimental data). On the other hand, they cannot form chain-like structures when immobilized in gel. It should also be noted that this effect is foreseen only for low anisotropy MNPs, i.e., when the energy barrier due to the magnetocristalline anisotropy is lower than the energy of the dipolar interactions [49].

In order to compare the heating efficiency as a function of the core size, data of Fig. 4 are reported in Fig. 5 for the agarose gel samples with 0.5% w/w for the three lowest frequencies. This comparison enlightens how the 14 nm sample is the most efficient at low frequencies, while moving to higher frequencies its *SAR* becomes progressively lower than the one of the 18 nm sample. Consequently, at frequencies higher than 330 kHz the obtained *SAR* trend is consistent with other findings in the literature [27] that reported an increase for core diameters approaching 20 nm. On the other hand, the highest *SAR* values for the 14 nm sample at the lowest frequency can be due to: (a) the narrower distribution of the MNPs core diameter compared to the other samples, caused by the "degradative influence of polydispersity" proved by Rosensweig in Ref.[8]; (b) the occurrence of a maximum in $\chi''(f)$ for the 14 nm sample nearer to 110 kHz with respect to the 18 nm sample case; (c) most probably, a mix of the hypotheses (a) and (b). We remind that $\chi''(f)$ reaches a maximum when the product $2\pi f\tau = 1$ [35], i.e., when the AMF frequency matches the effective relaxation time τ of the MNPs (see also Table 6), causing a maximum opening of the hysteresis loop.

4.4. LRT model and estimation of the effective relaxation time

The *SAR* vs H curves of Fig. 4 were fitted to a square law, i.e., $SAR(H) = \alpha H^2$, within the range of LRT validity, i.e., for $\xi = \mu_0 M_S V H_{max}/k_B T < 1$ [15]. It is worth noting that the 10 nm and 18 nm samples always and never satisfy this condition, respectively, while for the 14 nm sample $\xi < 1$ implies $H_{max} < (5.7 \pm 0.6)$ kA/m. In Fig. 4 this limit has been marked as a grey bar in the graphs. From the obtained parameter α, $\chi''(f)$ was evaluated according to Eq. (4) as $\chi''(f) = \alpha C/\mu_0 \pi f$.

The results obtained for the 14 nm sample showed a clear increase of $\chi''(f)$ when reducing the frequency in both conditions (solution and gel). We fitted these results according to Eq. (5) (curves not shown), using the experimental saturation magnetization M_{S_V}, the volume V of Tables 2 and 3, and setting the effective relaxation time τ as the only free parameter. The best fit curves of $\chi''(f)$ showed maxima at 25 kHz for the water sample and at 12 kHz for the gels. These values are lower than those reported in literature [25,52] for 14 nm MNPs, but the known strong dependence of $\chi''(f)$ from the polydispersity of the samples makes not meaningful a direct comparison.

The effective relaxation times in water (τ_{water}) and in agarose gels (τ_{gel}), obtained as best-fit parameters, are reported in Table 4. For both

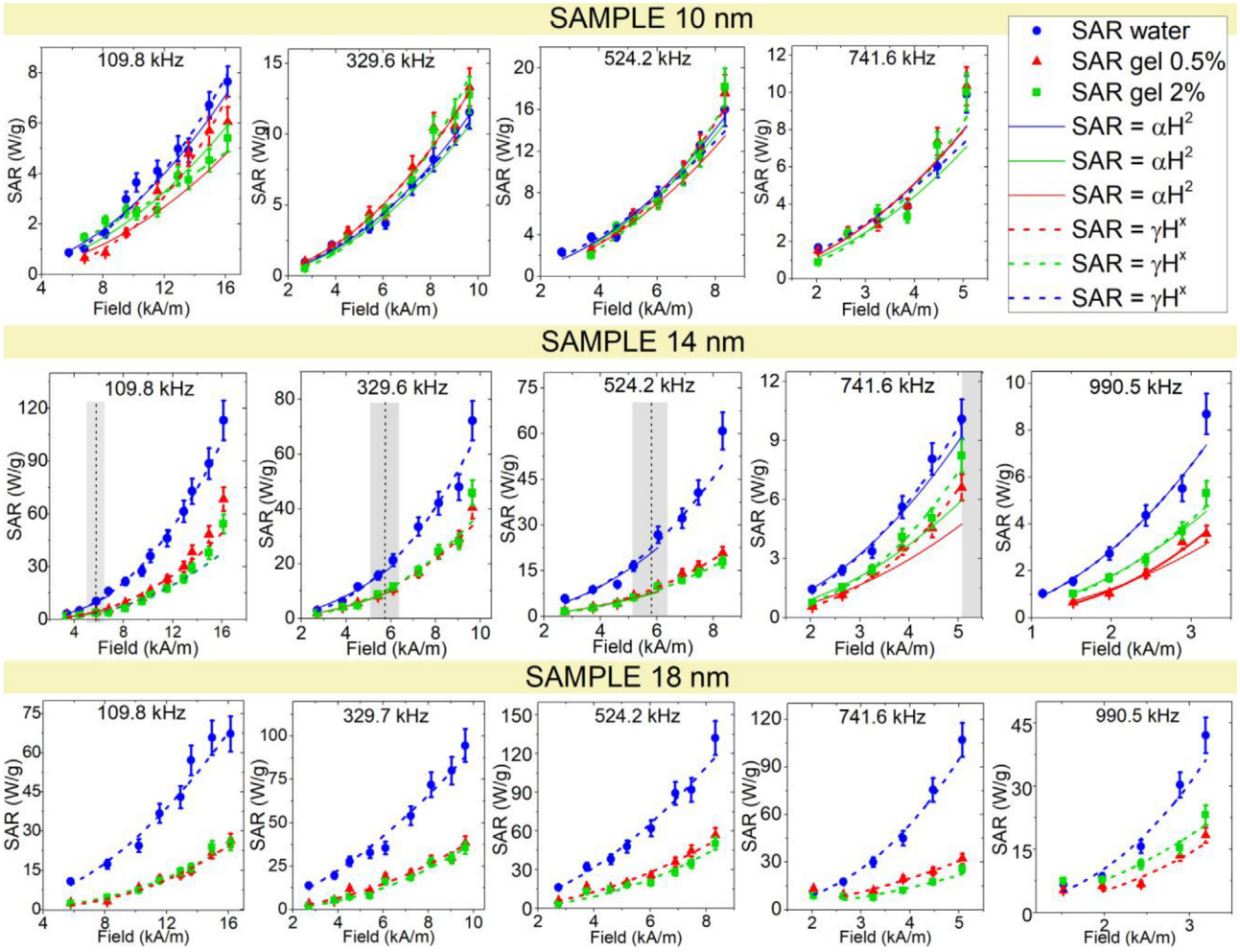

Fig. 4. *SAR* values obtained from Eq. (6) for the 10 nm, 14 nm and 18 nm samples, both in water and in agarose gel (0.5% and 2%) as a function of the applied AMF at different frequencies. Continuous lines represent the best-fits to the LRT model ($SAR(H) = \alpha H^2$) applied within its validity limits, i.e., the whole field range for the 10 nm sample and for values below the grey bar ones (representing the limit $\xi < 1$ with its uncertainty) for the 14 nm sample. Dotted lines denote the best-fitting curves obtained by applying the free-exponent model $SAR(H) = \beta H^x$.

samples $\tau_{gel}(0.5\%) \approx \tau_{gel}(2\%)$, while a significant difference between τ_{gel} and τ_{water} is observed only in the case of the 14 nm sample. Since the contribution of the Brownian relaxation mechanism is hindered in gel, we can assume $\tau_{gel} \approx \tau_N$. Considering $\tau_N = \tau_{gel}(0.5\%) = (1.35 \pm 0.21)\cdot 10^{-5}$ s for the 14 nm sample, the Brown relaxation time calculated by Eq. (3) assumes the value $\tau_B = (1.3 \pm 0.4)\cdot 10^{-5}$ s. As in this case $\tau_N \sim \tau_B$, the two physical mechanisms contribute almost equally to the heat release. However, this method suffers of severe limitations due to the approximations used for

Table 4
Effective relaxation times τ obtained by fitting the $\chi''(f)$ curves according to Eq. (5) for 10 and 14 nm samples in water solution and agarose gels.

	τ(s)[10nm]	τ(s)[14nm]
Aqueous solution	$(4.0 \pm 1.0)\cdot 10^{-8}$	$(6.5 \pm 1.1)\cdot 10^{-6}$
Agarose gel 0.5%	$(4.0 \pm 0.9)\cdot 10^{-8}$	$(1.35 \pm 0.21)\cdot 10^{-5}$
Agarose gel 2%	$(3.5 \pm 0.9)\cdot 10^{-8}$	$(1.34 \pm 0.30)\cdot 10^{-5}$

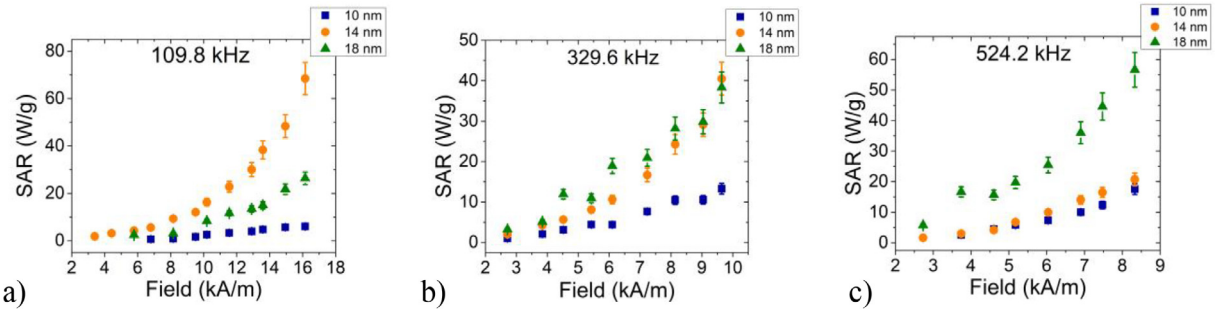

Fig. 5. *SAR* values obtained by Eq. (6) for the 10 nm, 14 nm and 18 nm samples in agarose gel at 0.5% as a function of the applied AMF at 109.8 kHz (a), 329.6 kHz (b) and 524.2 kHz (c). The 14 nm sample is the most efficient at the lowest frequency, while the 18 nm sample progressively improve its efficiency by increasing the frequency.

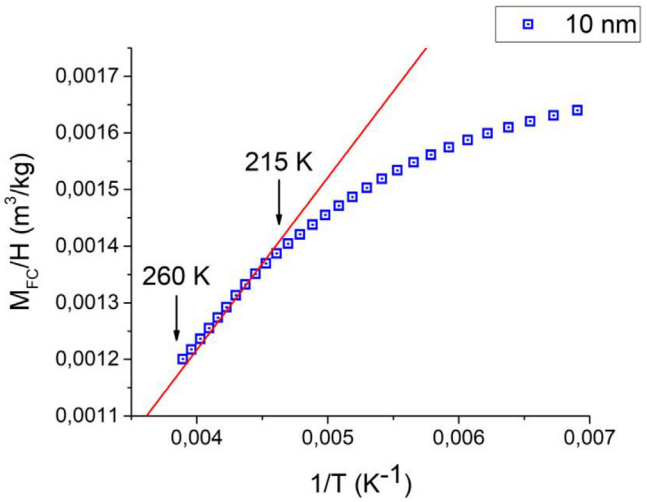

Fig. 6. Magnetization divided by the applied field as a function of the inverse temperature for the 10 nm sample. The linear trend observed between 260 K and 215 K demonstrates that the sample follow the Curie-Weiss law in the superparamagnetic regime.

estimating both $\chi''(f)$ and τ_N, and must be intended only as a complementary information about τ_B with respect to those obtained by other methods reported elsewhere [12,20,53,54]. These methods make use of accurate measurements of the physical parameters entering Eq. (2) [12] and of the AC magnetically-induced heating properties of viscous samples [20], of the modelling of the Brownian relaxation of MNPs in ferrofluids [53] by means of the Fokker–Planck equation, and of the magnetic spectroscopy of nanoparticles Brownian motion [54].

Another way to obtain a rough estimation of τ_N and τ_B (in water) for all the samples is to apply directly Eqs. (1) and (2) using the data known from the characterization of the samples. K_a in Eq. (1) is given by the relationship $K_a V \approx 25 k_B T_B$ [42]; here the blocking temperature T_B is deduced from the energy-barrier distribution obtained from ZFC-FC curves in frozen solutions by the derivative $-d(M_{FC}-M_{ZFC})/dT$ [7,12] (data not shown), and the core volume is estimated by the TEM data.

Before using the K_a values, we checked that the dipolar coupling can be neglected for all the samples. As shown by the M_{FC}/H vs 1/T plot in Fig. 6, the 10 nm sample satisfies the Curie-Weiss law in the superparamagnetic regime (red line). For the 14 nm and 18 nm samples, whose MNPs are blocked at 260 K, the only way to evaluate the dipolar energy is to apply the formula

$$E_{dip} \sim \frac{\mu_w}{4\pi} \cdot \frac{m^2}{\bar{d}^3} \tag{7}$$

where $\mu_w \sim 1.256627 \cdot 10^{-6}$ H/m is the magnetic permeability of the water, $m = M_S V \rho$ is the magnetic dipole of a single MNP at 260 K, $\rho = 5200$ kg/m^3 is the density of magnetite and $\bar{d}$ is the mean interparticle distance. Results are shown in Table 5; as can be seen, the ratio $E_{dip}/k_B T$ in water at 260 K is less than $1.2 \cdot 10^{-2}$ for all the samples.

Using the obtained values for K_a and V, and assuming $\tau_0 = 10^{-9}$ s and $T = 300$ K, it was possible to estimate τ_N. We also evaluated τ_B by setting $\eta = 1cP$ (i.e., as the water viscosity) in Eq. (2) and V_h as the volume obtained by the AFM. The results are shown in Table 6.

Comparing the values of τ obtained by applying Eqs. (1)–(3) (see Table 6) and by fitting the extrapolated $\chi''(f)$ curves (see Table 4), it could be noticed that the results of the two methods are not so far, in particular for the 14 nm sample, despite the rough approximations used in the two methods. Moreover, in both cases the results explain the measured *SAR* values, that result from the non-negligible or negligible contribution of τ_B to τ in liquid or gel samples, respectively.

Table 5
From the left: magnetite concentrations for the samples used in hyperthermia measurements; number #NP of MNPs within 1 mL; mean interparticle distance $\bar{d}$ for the 10 nm, 14 nm and 18 nm samples calculated at the same concentration; mean magnetic moment m of a single MNP; dipolar energy E_{dip} obtained from Eq. (7) using TEM and SQUID measurements; ratio between dipolar and thermal energies.

Sample	$[Fe_3O_4]$ (mg/mL)	#NP	$\bar{d}$ (nm)	m (A m^2)	E_{dip}water (J)	$\frac{E_{dip}}{k_B T}$water
10 nm	10	$2.92 \cdot 10^{15}$	70	$1.75 \cdot 10^{-19}$	$8.96 \cdot 10^{-24}$	$2.50 \cdot 10^{-3}$
14 nm	10	$1.28 \cdot 10^{15}$	92	$5.78 \cdot 10^{-19}$	$4.28 \cdot 10^{-23}$	$1.19 \cdot 10^{-2}$
18 nm	3	$1.92 \cdot 10^{14}$	173	$1.38 \cdot 10^{-18}$	$3.65 \cdot 10^{-23}$	$1.02 \cdot 10^{-2}$

Table 6
Anisotropy constant estimated from the ZFC-FC curves and Néel, Brown and effective relaxation times obtained from Eqs. (1)–(3). The relaxation times have been evaluated from TEM, AFM and SQUID measurements for samples in water solution.

Sample	K_a (J/m^3)	τ_N (s)	τ_B (s)	τ (s)
10 nm	$(3.2 \pm 0.8) \cdot 10^4$	$(1.6 \pm 2.7) \cdot 10^{-7}$	$(5.9 \pm 1.5) \cdot 10^{-7}$	$(1.3 \pm 1.6) \cdot 10^{-7}$
14 nm	$(2.7 \pm 0.3) \cdot 10^4$	$(2.1 \pm 3.3) \cdot 10^{-5}$	$(1.6 \pm 0.3) \cdot 10^{-6}$	$(1.4 \pm 0.3) \cdot 10^{-6}$
18 nm	$(1.1 \pm 0.3) \cdot 10^4$	$(2.6 \pm 7.4) \cdot 10^{-6}$	$(2.90 \pm 0.66) \cdot 10^{-6}$	$(1.4 \pm 2.1) \cdot 10^{-6}$

4.5. Validity of the LRT and Rayleigh models

It is important to discuss the applicability of the LRT model, used in the data analysis described in Section 4.4. Formally, we applied the LRT model in its validity range, but if we look at the fitting curves in Fig. 4 we see that in some cases it fails to describe the *SAR* vs *H* behaviour, particularly at high *H* amplitudes (for example for the 14 nm sample at 741.6 kHz). This discrepancy may be due to the fact that MNPs of these sizes, and particularly at high frequencies, are in the blocked regime. In similar conditions, the *SAR*(*H*) curve has been often described by a power law with an exponent greater than 2 [53,55] but lower than 3, as foreseen by the Rayleigh model for multidomain nanoparticles. In order to check this occurrence, the *SAR*(*H*) curves for all the samples in the whole frequency range were fitted to a free-exponent power-law model, i.e., $SAR(H) = \beta H^X$ [27]. The obtained best-fit curves (dashed lines in Fig. 4) show a better agreement between theory and experimental data with respect to the case $X = 2$.

The values of the free-exponents *X*, obtained from the fits for the three samples, both in water and in agarose gel, resulted to be generally greater than 2 and lower than 3, in agreement with the previous discussion. A clear dependence of the *X* values from the solvent composition or the particle diameter was not observed. These results highlight the need, already mentioned elsewhere [27], to theoretically investigate more in depth the mechanisms responsible for the heat release by single domain MNPs when the LRT is no more applicable ($\xi > 1$).

5. Conclusions

We investigated the hyperthermic behaviour of three samples of MNPs with magnetite core diameters of 10, 14 and 18 nm, dispersed both in aqueous solution and in agarose gels at concentrations 0.5% and 2%. The 10 nm sample shows similar heating efficiencies in both media; on the contrary, the 14 nm and 18 nm samples showed a relevant difference between the *SAR* values measured in water and in agarose gels, being higher the ones in water. For all the gel samples the heating efficiency resulted to be independent of the mass fraction.

Our results are in good agreement with the ones previously reported by de la Presa et al. [22] for maghemite nanoparticles, and can be explained on the basis of the immobilization of the MNPs suspended in gel and of the different role of Néel and Brown relaxation mechanisms in

the release of heat when the size of the MNPs core is changed [16,22]. Considering these outcomes, the common attitude to study MNPs only in aqueous solutions should be discouraged because it may evidently cause misleading conclusions about the real heating efficiency of MNPs when transferred to the clinics. In fact, in-gel studies of MNPs simulate the behaviour of MNPs in *in vivo* experiments (where they are injected in tissues, whose viscosity is similar to the one of gels) and should be considered complementary to the on cells *in vitro* ones, where aggregation processes frequently occurring in the biological culture medium affect the final results [56].

For the 10 nm and 14 nm samples, the LRT model was fitted to the $SAR(H)$ curves and the fit parameters were used to evaluate the effective relaxation times. Finally, a free-exponent model (i.e., $SAR = \beta H^X$) was fitted to all the $SAR(H)$ curves at different frequencies. For the 10 nm sample a good agreement between the data and the LRT model prediction (i.e., $X = 2$) was found, particularly in water. For the 14 and 18 nm samples the values of X, that fall in the range between 2 (typical of LRT) and 3 (Rayleigh model), highlight the necessity already mentioned elsewhere [15,27] of a new comprehensive model able to describe the evolution of SAR for single domain MNPs.

Acknowledgements

The authors thank the COST Action TD1402 (RADIOMAG), the INSTM-RL project MOTORSPORT, Fondazione Banca del Monte di Lombardia. The INFN HADROCOMBI and HADROMAG projects are acknowledged for partly funding the work.

References

[1] S. Dutz, R. Hergt, Magnetic particle hyperthermia – A promising tumour therapy? Nanotechnology. 25 (2014), https://doi.org/10.1088/0957-4484/25/45/452001.
[2] D. Ortega, Q.A. Pankhurst, Magnetic Hyperthermia 1 (2013) 60–88, https://doi.org/10.1039/9781849734844-00060.
[3] S. Laurent, S. Dutz, U.O. Häfeli, M. Mahmoudi, Magnetic fluid hyperthermia: Focus on superparamagnetic iron oxide nanoparticles, Adv. Colloid Interface Sci. 166 (2011) 8–23, https://doi.org/10.1016/j.cis.2011.04.003.
[4] Q.A. Pankhurst, N.K.T. Thanh, S.K. Jones, J. Dobson, Progress in applications of magnetic nanoparticles in biomedicine, J. Phys. D. Appl. Phys. 42 (2009), https://doi.org/10.1088/0022-3727/42/22/224001.
[5] R. Hergt, S. Dutz, R. Müller, M. Zeisberger, Magnetic particle hyperthermia: Nanoparticle magnetism and materials development for cancer therapy, J. Phys. Condens. Matter. 18 (2006), https://doi.org/10.1088/0953-8984/18/38/S26.
[6] E.A. Périgo, G. Hemery, O. Sandre, D. Ortega, E. Garaio, F. Plazaola, F.J. Teran, Fundamentals and advances in magnetic hyperthermia, Appl. Phys. Rev. 2 (2015), https://doi.org/10.1063/1.4935688.
[7] F. Burrows, A Model Of Magnetic Hyperthermia Submitted for the Degree of Master of Science, The University of York, Department of Physics (2012).
[8] R.E. Rosensweig, Heating magnetic fluid with alternating magnetic field, J. Magn. Magn. Mater. 252 (2002) 370–374, https://doi.org/10.1016/S0304-8853(02)00706-0.
[9] R. Hergt, S. Dutz, M. Zeisberger, Validity limits of the Néel relaxation model of magnetic nanoparticles for hyperthermia, Nanotechnology. 21 (2010) 15706, https://doi.org/10.1088/0957-4484/21/1/015706.
[10] B. Fischer, B. Huke, M. Lücke, R. Hempelmann, Brownian relaxation of magnetic colloids, J. Magn. Magn. Mater. 289 (2005) 74–77, https://doi.org/10.1016/j.jmmm.2004.11.021.
[11] M.I. Shliomis, V.I. Stepanov, Theory of the Dynamic Susceptibility of Magnetic Fluids, 2017. doi: 10.1002/9780470141465.ch1.
[12] E. Lima, E. De Biasi, R.D. Zysler, M. Vasquez Mansilla, M.L. Mojica-Pisciotti, T.E. Torres, M.P. Calatayud, C. Marquina, M. Ricardo Ibarra, G.F. Goya, Relaxation time diagram for identifying heat generation mechanisms in magnetic fluid hyperthermia, J. Nanoparticle Res. 16 (2014) 1–11, https://doi.org/10.1007/s11051-014-2791-6.
[13] R. Hergt, S. Dutz, M. Röder, Effects of size distribution on hysteresis losses of magnetic nanoparticles for hyperthermia, J. Phys. Condens. Matter. 20 (2008), https://doi.org/10.1088/0953-8984/20/38/385214.
[14] M. Coïsson, G. Barrera, F. Celegato, L. Martino, F. Vinai, P. Martino, G. Ferraro, P. Tiberto, Specific absorption rate determination of magnetic nanoparticles through hyperthermia measurements in non-adiabatic conditions, J. Magn. Magn. Mater. 415 (2016) 2–7, https://doi.org/10.1016/j.jmmm.2015.11.044.
[15] J. Carrey, B. Mehdaoui, M. Respaud, Simple models for dynamic hysteresis loop calculations of magnetic single-domain nanoparticles: Application to magnetic hyperthermia optimization, J. Appl. Phys. 109 (2011), https://doi.org/10.1063/1.3551582.
[16] R. Di Corato, A. Espinosa, L. Lartigue, M. Tharaud, S. Chat, T. Pellegrino, C. Ménager, F. Gazeau, C. Wilhelm, Magnetic hyperthermia efficiency in the cellular environment for different nanoparticle designs, Biomaterials. 35 (2014) 6400–6411, https://doi.org/10.1016/j.biomaterials.2014.04.036.
[17] D. Soukup, S. Moise, E. Céspedes, J. Dobson, N.D. Telling, In-situ measurement of magnetisation relaxation of internalised nanoparticles in live cells, ACS Nano (2015) 231–240, https://doi.org/10.1021/nn503888j.
[18] S. Dutz, M. Kettering, I. Hilger, R. Müller, M. Zeisberger, Magnetic multicore nanoparticles for hyperthermia-influence of particle immobilization in tumour tissue on magnetic properties, Nanotechnology. 22 (2011), https://doi.org/10.1088/0957-4484/22/26/265102.
[19] S. Moise, E. Céspedes, D. Soukup, J.M. Byrne, A.J. El Haj, N.D. Telling, The cellular magnetic response and biocompatibility of biogenic zinc- and cobalt-doped magnetite nanoparticles, Sci. Rep. 7 (2017) 1–11, https://doi.org/10.1038/srep39922.
[20] M. Jeun, Y.J. Kim, K.H. Park, S.H. Paek, S. Bae, Physical Contribution of Néel and Brown Relaxation to Interpreting Intracellular Hyperthermia Characteristics Using Superparamagnetic Nanofluids, J. Nanosci. Nanotechnol. 13 (2013) 5719–5725, https://doi.org/10.1166/jnn.2013.7524.
[21] V.S. Kalambur, B. Han, B.E. Hammer, T.W. Shield, J.C. Bischof, In vitro characterization of movement, heating and visualization of magnetic nanoparticles for biomedical applications, Nanotechnology 16 (2005) 1221–1233, https://doi.org/10.1088/0957-4484/16/8/041.
[22] P. De La Presa, Y. Luengo, M. Multigner, R. Costo, M.P. Morales, G. Rivero, A. Hernando, Study of heating efficiency as a function of concentration, size, and applied field in γ-Fe2O3 nanoparticles, J. Phys. Chem. C. 116 (2012) 25602–25610, https://doi.org/10.1021/jp310771p.
[23] G. Salas, J. Camarero, D. Cabrera, H. Takacs, M. Varela, R. Ludwig, H. Dähring, I. Hilger, R. Miranda, M.D.P. Morales, F.J. Teran, Modulation of magnetic heating via dipolar magnetic interactions in monodisperse and crystalline iron oxide nanoparticles, J. Phys. Chem. C. 118 (2014) 19985–19994, https://doi.org/10.1021/jp5041234.
[24] Y. Pineiro, Z. Vargas-Osorio, M. Banobre-Lopez, Y.V. Kolen'Ko, M.A. Lopez-Quintela, J. Rivas, Relevant parameters for magnetic hyperthermia in biological applications: agglomeration, concentration, and viscosity, IEEE Trans. Magn. 52 (2016) 18–21, https://doi.org/10.1109/TMAG.2016.2516645.
[25] G. Glöckl, R. Hergt, M. Zeisberger, S. Dutz, S. Nagel, W. Weitschies, The effect of field parameters, nanoparticle properties and immobilization on the specific heating power in magnetic particle hyperthermia, J. Phys. Condens. Matter. 18 (2006), https://doi.org/10.1088/0953-8984/18/38/S27.
[26] B. Mehdaoui, A. Meffre, J. Carrey, S. Lachaize, L.M. Lacroix, M. Gougeon, B. Chaudret, M. Respaud, Optimal size of nanoparticles for magnetic hyperthermia: a combined theoretical and experimental study, Adv. Funct. Mater. 21 (2011) 4573–4581, https://doi.org/10.1002/adfm.201101243.
[27] M. Cobianchi, A. Guerrini, M. Avolio, C. Innocenti, M. Corti, P. Arosio, F. Orsini, C. Sangregorio, A. Lascialfari, Experimental determination of the frequency and field dependence of specific loss power in magnetic fluid hyperthermia, J. Magn. Magn. Mater. 444 (2017) 154–160, https://doi.org/10.1016/j.jmmm.2017.08.014.
[28] G. Vallejo-Fernandez, O. Whear, A.G. Roca, S. Hussain, J. Timmis, V. Patel, K. O'Grady, Mechanisms of hyperthermia in magnetic nanoparticles, J. Phys. D. Appl. Phys. 46 (2013), https://doi.org/10.1088/0022-3727/46/31/312001.
[29] M. Salloum, R.H. Ma, D. Weeks, L. Zhu, Controlling nanoparticle delivery in magnetic nanoparticle hyperthermia for cancer treatment: Experimental study in agarose gel, Int. J. Hyperth. 24 (2008) 337–345, https://doi.org/10.1080/02656730801907937.
[30] E. Fernández, D. López, C. Mijangos, M. Duskova-Smrckova, M. Ilavsky, K. Dusek, Rheological and thermal properties of agarose aqueous solutions and hydrogels, J. Polym. Sci. Part B Polym. Phys. 46 (2008) 322–328, https://doi.org/10.1002/polb.21370.
[31] K. Lahrech, A. Safouane, J. Peyrellasse, Sol state formation and melting of agar gels rheological study, Phys. A Stat. Mech. Appl. (2005) 205–211, https://doi.org/10.1016/j.physa.2005.06.022.
[32] I.A. Brezovich, Low frequency hyperthermia: capacitive and ferromagnetic thermoseed methods, Med. Phys. Monogr. No 16 Biol. Phys. Clin. Asp. Hyperth., 1988: pp. 82–110.
[33] R. Hergt, S. Dutz, Magnetic particle hyperthermia-biophysical limitations of a visionary tumour therapy, J. Magn. Magn. Mater. 311 (2007) 187–192, https://doi.org/10.1016/j.jmmm.2006.10.1156.
[34] M. Zhang, Z. Che, J. Chen, H. Zhao, L. Yang, Z. Zhong, J. Lu, Experimental determination of thermal conductivity of water-agar gel at different concentrations and temperatures, J. Chem. Eng. Data. 56 (2011) 859–864, https://doi.org/10.1021/je100570h.
[35] A. Urtizberea, E. Natividad, A. Arizaga, M. Castro, A. Mediano, Specific absorption rates and magnetic properties of ferrofluids with interaction effects at low concentrations, J. Phys. Chem. C. 114 (2010) 4916–4922, https://doi.org/10.1021/jp912076f.
[36] G.S. Pawley, Unit-cell refinement from powder diffraction scans, J. Appl. Crystallogr. 14 (1981) 357–361, https://doi.org/10.1107/S0021889881009618.
[37] A.A. Coelho, Topas, General profile and structure analysis software for powder diffraction Data, Bruker AXS (2005).
[38] J.L. Dormann, L. Bessais, D. Fiorani, A dynamic study of small interacting particles: Superparamagnetic model and spin-glass laws, J. Phys. C Solid State Phys. 21 (1988) 2015–2034, https://doi.org/10.1088/0022-3719/21/10/019.
[39] J.L. Dormann, D. Fiorani, E. Tronc, On the models for interparticle interactions in nanoparticle assemblies: comparison with experimental results, J. Magn. Magn. Mater. 202 (1999) 251–267, https://doi.org/10.1016/S0304-8853(98)00627-1.
[40] S. Soeya, J. Hayakawa, H. Takahashi, K. Ito, C. Yamamoto, A. Kida, H. Asano, M. Matsui, Development of half-metallic ultrathin Fe3O4films for spin-transport

devices, Appl. Phys. Lett. 80 (2002) 823–825, https://doi.org/10.1063/1.1446995.
[41] A.G. Kolhatkar, A.C. Jamison, D. Litvinov, R.C. Willson, T.R. Lee, Tuning the magnetic properties of nanoparticles, Int. J. Mol. Sci. (2013), https://doi.org/10.3390/ijms140815977.
[42] G.F. Goya, T.S. Berquò, F.C. Fonseca, M.P. Morales, Static and dynamic magnetic properties of spherical magnetite nanoparticles, J. Appl. Phys. 94 (5) (2003) 3520–3528, https://doi.org/10.1063/1.1599959.
[43] H. Gavilán, O. Posth, L.K. Bogart, U. Steinhoff, L. Gutiérrez, M.P. Morales, How shape and internal structure affect the magnetic properties of anisometric magnetite nanoparticles, Acta Mater. 125 (2017) 416–424, https://doi.org/10.1016/j.actamat.2016.12.016.
[44] R. Aragan, D.J. Buttrey, J.P. Shepherd, J.M. Honig, Influence of nonstoichiometry on the Verwey transition, Phys. Rev. B. 31 (1985) 430–436, https://doi.org/10.1103/PhysRevB.31.430.
[45] F. Walz, The Verwey transition - a topical review, J. Phys. C Condens. Matter. 14 (2002) R285, https://doi.org/10.1088/0953-8984/14/12/203.
[46] G.E.P. Box, H.L. Lucas, Design of Experiments in Non-Linear Situations, Biometrika. 46 (1959) 77, https://doi.org/10.2307/2332810.
[47] C. Blanco-Andujar, D. Ortega, P. Southern, Q.A. Pankhurst, N.T.K. Thanh, High performance multi-core iron oxide nanoparticles for magnetic hyperthermia: microwave synthesis, and the role of core-to-core interactions, Nanoscale. 7 (2015) 1768–1775, https://doi.org/10.1039/C4NR06239F.
[48] A. Cervadoro, C. Giverso, R. Pande, S. Sarangi, L. Preziosi, J. Wosik, A. Brazdeikis, P. Decuzzi, Design maps for the hyperthermic treatment of tumors with superparamagnetic nanoparticles, PLoS One 8 (2013) 1–14, https://doi.org/10.1371/journal.pone.0057332.
[49] B. Mehdaoui, R.P. Tan, A. Meffre, J. Carrey, S. Lachaize, B. Chaudret, M. Respaud, Increase of magnetic hyperthermia efficiency due to dipolar interactions in low-anisotropy magnetic nanoparticles: Theoretical and experimental results, Phys. Rev. B – Condens. Matter Mater. Phys. 87 (2013) 1–10, https://doi.org/10.1103/PhysRevB.87.174419.
[50] L.C. Branquinho, M.S. Carrião, A.S. Costa, N. Zufelato, M.H. Sousa, R. Miotto, R. Ivkov, A.F. Bakuzis, Effect of magnetic dipolar interactions on nanoparticle heating efficiency: Implications for cancer hyperthermia, Sci. Rep. 3 (2013) 20–22, https://doi.org/10.1038/srep02887.
[51] D. Serantes, K. Simeonidis, M. Angelakeris, O. Chubykalo-Fesenko, M. Marciello, M. Del Puerto Morales, D. Baldomir, C. Martinez-Boubeta, Multiplying magnetic hyperthermia response by nanoparticle assembling, J. Phys. Chem. C 118 (2014) 5927–5934, https://doi.org/10.1021/jp410717m.
[52] R. Hergt, S. Dutz, R. Müller, M. Zeisberger, Magnetic particle hyperthermia: Nanoparticle magnetism and materials development for cancer therapy, J. Phys. Condens. Matter. 18 (2006) 2919–2934, https://doi.org/10.1088/0953-8984/18/38/S26.
[53] M. Martens, R. Deissler, Y. Wu, B. Lisa, Z. Yao, B. Robert, G. Mark, Modeling the Brownian relaxation of nanoparticle ferrofluids: Comparison with experiment, 22303, 2013 Int. Work. Magn. Part. Imaging, IWMPI 2013, 2013, https://doi.org/10.1109/IWMPI.2013.6528349.
[54] I.M. Perreard, D.B. Reeves, X. Zhang, E. Kuehlert, E.R. Forauer, J.B. Weaver, Temperature of the magnetic nanoparticle microenvironment: Estimation from relaxation times, Phys. Med. Biol. 59 (2014) 1109–1119, https://doi.org/10.1088/0031-9155/59/5/1109.
[55] A. Wijaya, K.A. Brown, J.D. Alper, K. Hamad-Schifferli, Magnetic field heating study of Fe-doped Au nanoparticles, J. Magn. Magn. Mater. 309 (2007) 15–19, https://doi.org/10.1016/j.jmmm.2006.04.014.
[56] D. Eberbeck, M. Kettering, C. Bergemann, P. Zirpel, I. Hilger, L. Trahms, Quantification of the aggregation of magnetic nanoparticles with different polymeric coatings in cell culture medium, J. Phys. D. Appl. Phys. 43 (2010), https://doi.org/10.1088/0022-3727/43/40/405002.